Chemical Engineering Journal 493 (2024) 152529

Contents lists available at ScienceDirect

Chemical Engineering Journal

journal homepage: www.elsevier.com/locate/cej

Room-temperature phosphorescence of defect-engineered silica nanoparticles for high-contrast afterglow bioimaging

Heemin Chang [a,b,1], Yoonsang Park [a,c,1], Kyunghwan Kim [d,1], Chaewon Han [e,f,1], Yeongjun Yoon [g], Woojung Yoo [h], Jounghyun Yoo [h], Dajin Lee [e,f], Hyunho Han [f], Kyeounghak Kim [g,*], Jinmyoung Joo [h,i,j,k,*], Woosung Kwon [a,e,*]

[a] Institute of Advanced Materials and Systems, Sookmyung Women's University, Seoul 04310, South Korea
[b] Department of Materials Engineering, The University of Tokyo, Tokyo 113-8656, Japan
[c] Nano Convergence Technology Research Center, Korea Electronics Technology Institute (KETI), Seongnam 13509, South Korea
[d] Department of Chemistry, Ulsan National Institute of Science and Technology (UNIST), Ulsan 44919, South Korea
[e] Department of Chemical and Biological Engineering, Sookmyung Women's University, Seoul 04310, South Korea
[f] Department of Urology, Urological Science Institute, Yonsei University College of Medicine, Seoul 03722, South Korea
[g] Department of Chemical Engineering, Hanyang University, Seoul 04763, South Korea
[h] Department of Biomedical Engineering, Ulsan National Institute of Science and Technology (UNIST), Ulsan 44919, South Korea
[i] Center for Genomic Integrity, Institute for Basic Science, Ulsan 44919, South Korea
[j] Graduate School of Health Science and Technology, Ulsan National Institute of Science and Technology (UNIST), Ulsan 44919, South Korea
[k] Materials Research Science and Engineering Center, University of California, San Diego, La Jolla, CA 92093, United States

ARTICLE INFO

Keywords:
Room-temperature phosphorescence
Defect engineering
Silica nanoparticle
Time-gated imaging
Tumor-targeting nanomedicine

ABSTRACT

Room-temperature phosphorescence (RTP) has tremendous potential in optics and photonics. Unlike fluorescence, RTP has substantial afterglow signals even after the excitation light is removed, which allows for extended acquisition times and higher signal-to-noise ratio under time-gated bioimaging. However, conventional RTP materials, both metal-containing and metal-free organic compounds, typically have limited photostability and inherent toxicity, making them unsuitable for long-term biological applications. Here, we report metal- and organic fluorophore-free silica nanoparticles (SNPs) that facilitate long-lived phosphorescence and exhibit RTP for high-contrast bioimaging. Polycondensation of silicon precursors and silyl biphenyls forms biphenyl-doped SNPs (bSNPs), and thermal decomposition of biphenyl moieties generates optically active defects in the biphenyl-bonded silicate network. The calcined bSNPs (C-bSNPs) have RTP-related biphenyl defects composed of carbon impurities, corresponding to spectroscopic measurements and ab initio calculations. Facile surface functionalization of defect-engineered C-bSNPs with tumor-targeting peptides while maintaining long-lived RTP allows for tissue autofluorescence-free in vivo bioimaging for cancer diagnosis, surpassing the limitations of continuous-wave imaging.

1. Introduction

Upon light absorption in semiconducting materials, electrons are excited from their fundamental ground state (S_0) to a singlet excited state (S_n), and the photoexcited electrons are spontaneously transited to the lowest excited (S_1) state via internal conversion. Fluorescence is a radiative de-excitation process from the excited state (S_1) to the ground state (S_0) to stabilize the energy level as a form of light emission [1,2]. Occasionally, the photoexcited electrons undergo spin conversion to the triplet (T_1) state through intersystem crossing (ISC), followed by radiative de-excitation to the ground state (S_0) [3]. This process called phosphorescence exhibits extended emissive decay lifetimes in the range of milliseconds to hours, in contrast to fluorescence which lasts for nanoseconds. Hence, phosphorescence is of considerable interest in

* Corresponding authors at: Department of Chemical Engineering, Hanyang University, Seoul 04763, South Korea (K. Kim). Department of Biomedical Engineering, Ulsan National Institute of Science and Technology (UNIST), Ulsan 44919, South Korea (J. Joo). Institute of Advanced Materials and Systems, Sookmyung Women's University, Seoul 04310, South Korea (W. Kwon).
E-mail addresses: chemekim@hanyang.ac.kr (K. Kim), jjoo@unist.ac.kr (J. Joo), wkwon@sookmyung.ac.kr (W. Kwon).
[1] These authors contributed equally to this work.

https://doi.org/10.1016/j.cej.2024.152529
Received 12 February 2024; Received in revised form 18 May 2024; Accepted 23 May 2024
Available online 24 May 2024

optoelectronics [4–7], anticounterfeiting [8], and biological imaging [9–13]. However, phosphorescence is typically observed at extremely low temperature, which significantly limits its practical application.

In this regard, room-temperature phosphorescence (RTP) has attracted significant attention over the past few decades [14,15]. Rare-earth metals are used as a key component for RTP materials to facilitate ISC; however, they have several disadvantages including high cost, acute toxicity, and reduced stability against moisture. To develop metal-free RTP materials, various photo-active materials such as organic fluorophores and supramolecular structures have been adopted and extensively investigated [16–25]. The general strategy for achieving metal-free RTP involves suppressing the organic fluorophore vibrations to restrict the nonradiative thermal decay pathways, thereby facilitating the triplet state radiative decay [26–30]. As such, metal-free RTP is typically observed in rigid structures (crystalline states or solid-state blends) that can effectively suppress vibration. To date, several RTP materials have been developed by embedding fluorophores in host matrices such as poly(methyl methacrylate), poly(vinyl alcohol), and silica [10,31–35].

One of the attractive biomedical applications of RTP materials is employing them as a luminescent probe in imaging-guided diagnostics, which allows for noninvasive detection of diseases such as cancer and infection [36–42]. The long-lived excited state of RTP enables to facilitate the precise tracking of the luminescent probes with time-gated imaging systems, in which short-lived tissue autofluorescence is completely eliminated, thereby resulting in background-free bioimaging [43]. However, realizing long-lived RTP in aqueous phases remains challenging owing to the high dissolved oxygen concentration in water and free molecular motion, both of which results in RTP quenching of triplet excitons [44]. Furthermore, the use of typical organic fluorophore-based RTP in bioimaging is limited because of the possibility of fluorophore leakage from the host matrix and lack of long-term stability [45,46]. Therefore, a novel design strategy for metal- and organic-fluorophore-free materials is necessary, particularly to achieve water-stable RTP for high-contrast bioimaging.

Herein, we report defect-engineered silica nanoparticles (SNPs) that exhibit unprecedentedly noticeable RTP without use of metal activators or organic fluorophores. Using silyl biphenyls as an additive to the Stöber method producing SNPs, the biphenyl-doped silica nanoparticles (bSNPs) are readily synthesized, which are then calcined at high temperature. Thermal decomposition of the biphenyl groups during the calcination process generates optically active defects in the silicate

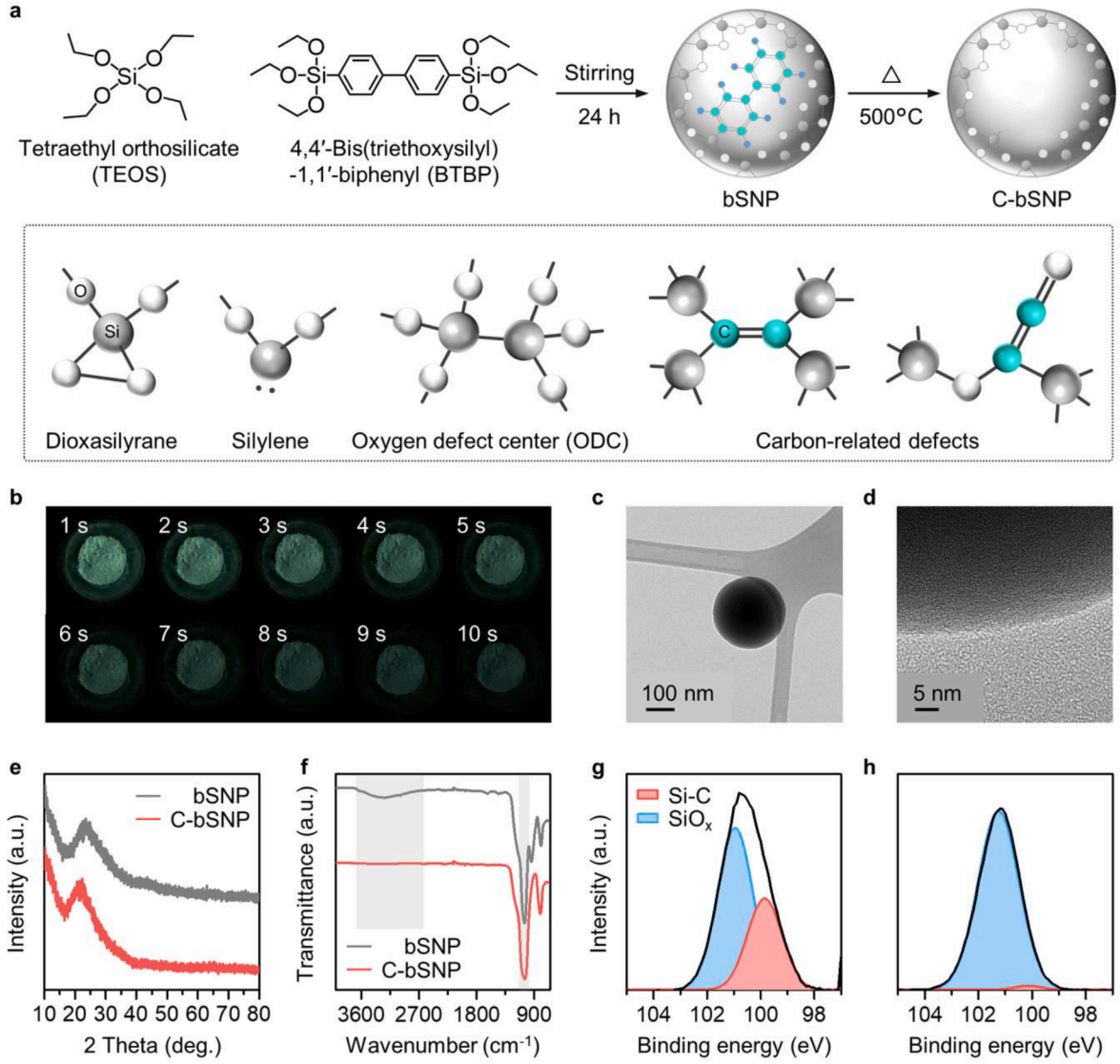

Fig. 1. Chemical structure and characteristics of C-bSNPs. (a) Schematic illustration depicting synthesis process of bSNPs and C-bSNPs, and corresponding chemical structures in the defects. (b) Photographic images of C-bSNPs after ceasing UV (365 nm) irradiation under ambient condition at room-temperature. (c) TEM and (d) HRTEM images of C-bSNPs. (e) XRD patterns and (f) ATR-FTIR spectra of bSNPs and C-bSNPs. High-resolution XPS spectra of Si 2p of (g) bSNPs and (h) C-bSNPs.

network, which is the origin of ISC inducing RTP. The large steric hindrance of the biphenyl groups in the bSNPs is responsible for the optical defects in the calcined bSNPs (C-bSNPs). Controlled calcination process is demonstrated to reveal the stable RTP of C-bSNPs, in which the nature of the defect structure is thoroughly investigated including spectroscopy and ab initio calculations. Facile surface chemistry of the C-bSNPs allows biochemical modification with a tumor-homing peptides to target cancer cells in vitro and in vivo. Finally, tumor-homing C-bSNPs show great biocompatibility and a novel diagnostic capability that clearly visualizes cancer with high-contrast using in vivo tissue autofluorescence-free bioimaging system.

2. Results and discussion

2.1. Morphological and chemical structures of C-bSNPs

To synthesize the C-bSNPs, we first prepared bSNPs as intermediates via the polycondensation of tetraethyl orthosilicate (TEOS) and 4,4′-bis (triethoxysilyl)-1,1′-biphenyl (BTBP). With the introduction of BTBP into the modified Stöber method, generation of specific silica defect sites was expected within the bSNPs owing to the large steric hindrance of the biphenyls (Fig. 1a). Subsequently, the bSNPs were placed in a muffle furnace and heated at 500 °C for 8 h to yield defect-engineered C-bSNPs. The resulting C-bSNPs powders emitted strong phosphorescence lasting several seconds after ultraviolet (UV) radiation in room-temperature (Fig. 1b and Movie S1), which was sufficiently bright to be seen by the naked eyes. Transmission electron microscopy (TEM) showed that the bSNPs exhibited narrow size distribution centered at ~320 nm in diameter with a uniformly spherical morphology (Fig. S1a and b). The C-bSNPs maintained spherical shape and size after the calcination process (Fig. 1c), ensuring the morphological stability while retaining the original size determined by the modified Stöber method. It should be also noted that the high-resolution TEM (HRTEM) showed that the nanoparticles (NPs) exhibited amorphous structures both prior to and post heat treatment (Fig. 1d and S1c). X-ray diffraction (XRD) analysis was further performed to determine the crystal structures of the bSNPs and C-bSNPs, and both XRD patterns exhibited broad diffraction spectra with a wide peak centered at $2\theta = 23^{\circ}$ (Fig. 1e), suggesting amorphous silica formation, corresponding to the HRTEM. Thus, neither the presence of the co-precursor (BTBP) nor the calcination process affected the crystalline structure of the silica NPs.

Attenuated total reflectance Fourier transform infrared (ATR-FTIR) spectroscopy was then performed to investigate the chemical structure of the synthesized SNPs (Fig. 1f). The ATR-FTIR spectra exhibited vibration peaks corresponding to Si–O–Si asymmetric (approximately 1053 cm^{-1}) and symmetric (approximately 800 cm^{-1}) stretching, thus confirming that the primary component of the NPs was the silica matrix. However, the signals corresponding to the Si–OH asymmetric bending (approximately 1631 cm^{-1}) and stretching (approximately 940 cm^{-1}) and OH bending (approximately 1450 cm^{-1}) and stretching (3500–3000 cm^{-1}) were diminished after calcination. The significant reduction in the number of hydroxide groups suggests the elimination of surface silanol groups during calcination.

X-ray photoelectron spectroscopy (XPS) analysis determined the elemental composition of the b-SNPs and C-bSNPs to reveal the calcination effects on the chemical structure of silica. The survey spectra of both bSNPs and C-bSNPs showed evident O 1s, C 1s, Si 2s, and Si 2p signals (Fig. S2a), and the high-resolution XPS spectra of Si 2p of the bSNPs and C-bSNPs showed the transition of Si-C to SiOx after calcination (Fig. 1g and h). The Si 2p pattern of the bSNPs exhibited a peak (with a binding energy of 100.7 eV) that could be deconvoluted into two peaks, with an intense peak at 99.8 eV corresponding to the Si atoms of the silicate (Si–Cs) groups and a comparatively less intense peak at 100.9 eV corresponding to the Si atoms of the SiOx groups. In comparison, the XPS patterns of the C-bSNPs positively shifted by approximately 0.5 eV as the number of Si atoms in the SiOx groups increased and that in the silicate decreased. The high-resolution XPS spectra of C 1s of both the bSNPs and C-bSNPs (Fig. S2b) showed C=C peaks (283.9 eV and 283.0 eV), a C–C and C–H bonding peak (286.4 eV) of biphenyl groups, and a C–Si bonding peak (282.5 eV). However, the overall C content decreased after calcination, indicating the calcination-induced destruction of biphenyl groups which are chemically bound to the silica matrix. The XPS patterns of O 1s suggest that the O content increased by approximately 1.7 times after calcination because the Si atoms, which became unstable owing to Si–C bond breakage, was combined with oxygen during calcination in air (Fig. S2c). The bSNPs exhibited a peak at 529.8 eV and a shoulder at 530.6 eV, whereas the C-bSNPs exhibited a peak at approximately 530.4 eV. This indicates that the O–Si groups (529.5 eV) were significantly reduced and that the number of Si–O–Si groups (530.7 eV) increased. The reduction in the O–Si groups is assumed to be associated with the reduction in the number of Si–OH groups induced by calcination. To further analyze the chemical structure, thermogravimetric analysis (TGA) and gas chromatography (GC) were also performed. The mass of the bSNPs drastically decreased until the temperature rose to approximately 175 °C owing to the evaporation of the absorbed water within the sample (Fig. S3a). Subsequently, no change in the mass was observed until 250 °C, and the mass decreased again from 250 °C to 500 °C. Mass spectroscopy combined with GC (GC/MS) was conducted on the gas generated within this range, and the chemical substances, such as benzaldehyde and 4-acryloylphenol, are responsible for the thermal decomposition of biphenyl groups (Fig. S3b).

2.2. Optical properties of C-bSNPs

The effect of calcination was further examined using UV–visible (UV–Vis) absorption spectroscopy (Fig. 2a). For the bSNPs, an absorption band was observed at ~265 nm, attributed to the $\pi \rightarrow \pi^*$ transition in the biphenyl benzenes, while the peak was diminished for the C-bSNPs, indicating the thermal decomposition of biphenyls. As the binding states were altered by calcination, the bSNPs and C-bSNPs exhibited different optical properties, thus we further investigated the influence of organic molecules and silica defects in the silica matrix in terms of the fluorescence properties. The fluorescence emission (FL_{em})

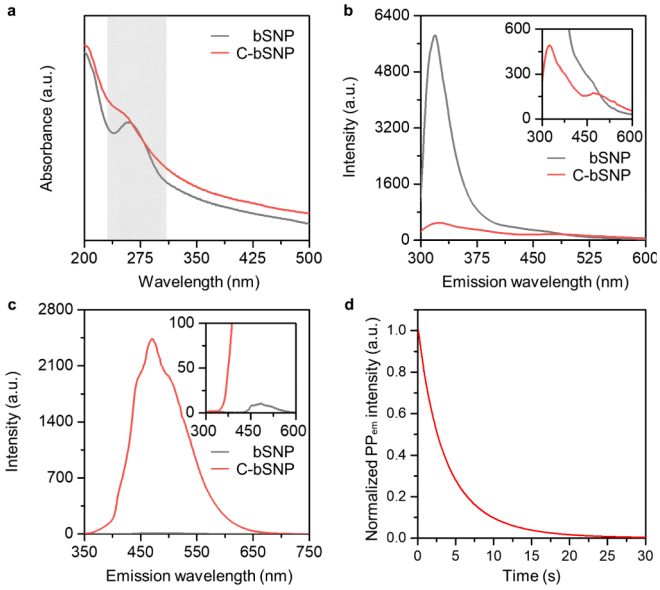

Fig. 2. Optical properties of C-bSNPs. (a) UV–Vis absorbance spectra of bSNPs and C-bSNPs. (b) FL_{em} spectra (λ_{ex} = 270 nm) and (c) PP_{em} spectra (λ_{ex} = 230 nm) of bSNPs and C-bSNPs, respectively. The magnified FL_{em} and PP_{em} spectra in the range of 300–600 nm are shown in the insets. (d) TRPL signal of C-bSNPs in the phosphorescence time domain (λ_{ex} = 264 nm; λ_{em} = 480 nm). Note that a.u. stands for arbitrary unit.

intensity, measured at an excitation wavelength (λ_{ex}) of 270 nm, decreased after calcination (Fig. 2b). Based on a comparison with the FL_{em} spectrum of the precursor BTBP (Fig. S4), the FL_{em} band at 320 nm was evidently from the biphenyl molecules. Because this energy state is typically destroyed after calcination, it is reasonable to infer that the biphenyl molecule did not significantly contribute to the FL_{em} of the C-bSNPs. The FL_{em} peak at approximately 470 nm did not significantly decrease after calcination but slightly increased (Fig. 2b). Given that the silylene and dioxasilyrane defect pairs contribute to the development of excitation bands at 245 nm and 370 nm, respectively [47], the fluorescence excitation (FL_{ex}) spectra were examined at an emission wavelength (λ_{em}) of 470 nm. As indicated in Fig. S5a, these excitation bands became relatively notable after calcination. This indicates that defect pairs were generated by the thermal degradation of biphenyls at 500 °C and that these defects primarily affected the 470 nm FL_{em} of the C-bSNPs. Phosphorescence spectroscopic analysis indicates that the C-bSNPs exhibited strong phosphorescence emission (PP_{em}) ranging from approximately 450 to 500 nm (Fig. 2c), which is related to the phosphorescence excitation (PP_{ex}) peak at 275 nm (Fig. S5b). Because such PP_{em} was almost unobserved in the bSNPs, it could be proposed that the structural and chemical transition of the silica matrix induced by calcination leads the ISC of photoexcited to triplet states.

To investigate the effects of the biphenyl co-precursor, SNPs were synthesized without BTBP, and calcined at identical condition with the C-bSNPs to prepare the C-SNPs. UV–Vis absorption spectra showed no significant difference prior to and after calcination (Fig. S6a), due to absence of the π-bonding components in the silica matrix. Furthermore, negligible FL_{em} and PP_{em} were observed for both the SNPs and C-SNPs (Fig. S6b–e). The results emphasize that the unique optical properties of the C-bSNPs were inferred to be related to the structural changes resulting from the thermal decomposition of the biphenyl groups. Markedly weak PP_{em} signal observed for the C-SNPs is presumably due to intrinsic carbon moieties, such as ethoxy groups from TEOS or carbon substances from air, which turned to structural changes with the thermal decomposition.

Time-resolved photoluminescence (TRPL) spectroscopy was performed to investigate the radiative recombination dynamics. TRPL signals of the bSNPs and C-bSNPs were measured in the fluorescence time domain of 0–50 ns (Fig. S7). The choice of λ_{ex} (264 nm and 374 nm) and λ_{em} (360 nm and 480 nm) aimed to closely align with the wavelengths corresponding to the energies of biphenyl-related states and silica defect-related states, respectively. The average FL_{em} lifetime (t_{avg}) of the particles under the probe wavelengths related to the biphenyl-related states remained unchanged after calcination (Table S1 and Fig. S7a), indicating that no spin–orbit coupling occurred in the remaining biphenyl molecules of the C-bSNPs. This implies that the ISC of the biphenyls to the triplet state was significantly unfavorable and that the phosphorescence of the C-bSNPs did not originate from the biphenyls. In contrast, increased FL_{em} lifetime was observed after calcination under the probe wavelengths corresponding to silica defect-related states (Table S1 and Fig. S7b), indicating that the fluorescence energy states increased owing to silica defect formation. To investigate the phosphorescence carrier dynamics and lifetime, TRPL signals of the C-bSNPs in the phosphorescence time domain of 0–30 s were measured at λ_{ex} = 264 nm and λ_{ex} = 480 nm (corresponding to the PP_{em} peak wavelength), as depicted in Fig. 2d. The average PP_{em} lifetime was determined as 3.8 s through a single exponential fit. Furthermore, the quantum yield was measured to be 26.51 % at λ_{ex} = 270 nm using an integrating sphere instrument, comparable to that of transition metal complexes and organic fluorophores. To the best of our knowledge, the defect structure of silica corresponding to this phosphorescence energy state has not been previously investigated.

2.3. Physicochemical origin of phosphorescence in C-bSNPs

Extensive investigations were further conducted to verify the origin of long-lived phosphorescence. First, hydrolysis experiments were performed to reveal the influence of the silica network and embedded organic species (e.g., biphenyl) molecular defects on the optical characteristics. Silica structures readily decompose through hydrolysis under alkaline condition, particularly at high pH [48]. Because the C-bSNPs predominantly comprise Si–O bonds, the luminescent characteristics are changed upon exposure to an alkaline solution containing NaOH.

To decompose the Si–O network and remove the embedded organic species, the C-bSNPs were treated with a NaOH solution (pH ~14) for 20 min. During this process, the Si–O bonds were cleaved by excessive hydroxyl ions at high pH, and the embedded organic species such as biphenyls were released from the silica network. Subsequently, the released organic species were separated from the product by centrifugation, leaving only the silica pellet (NaOH-treated C-bSNP) to be collected. The fluorescence spectra of the NaOH-treated C-bSNP show a significant decrease at 320 nm, corresponding to the BTBP fluorescence peak, confirming the removal of embedded biphenyl molecules (Fig. S8a). In addition, Raman spectrum of C-bSNPs detected only background luminescence signals and no signal appeared in the D and G band regions, indicating the absence of crystalline carbonaceous species (Fig. S8b). Consequently, the potential contribution of the biphenyl groups or organic species to the optical properties could be completely ruled out through this experiment.

The FL_{em} spectra measured at λ_{ex} = 370 nm, which is closer to the excitation band of the silica defects, further support the association of

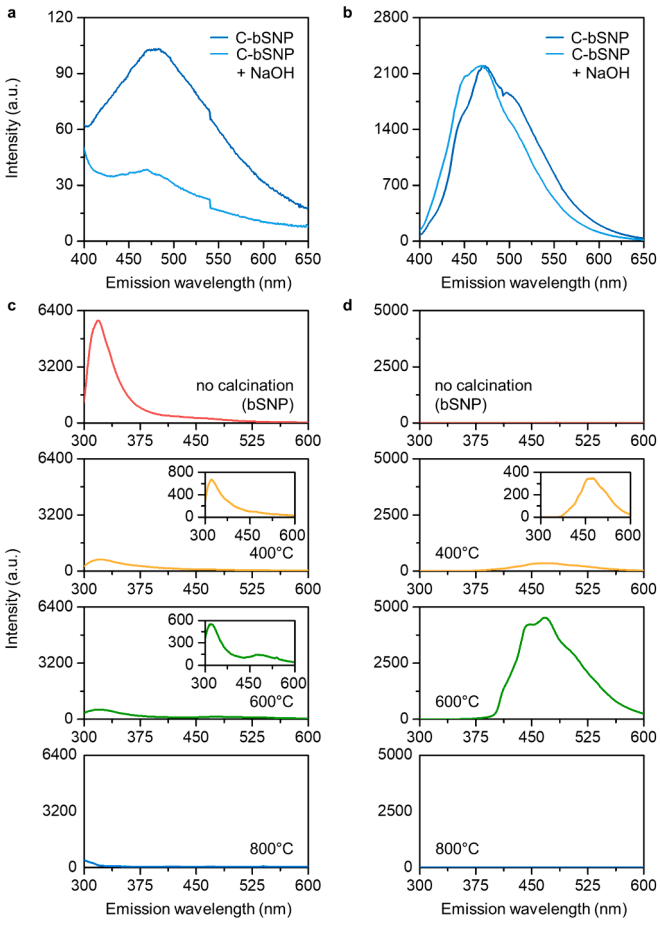

Fig. 3. Effect of NaOH addition and calcination temperature. (a) FL_{em} spectra (λex = 270 nm) of C-bSNPs before and 20 min after the addition of NaOH solution. (b) PPem spectra (λex = 230 nm) of C-bSNPs before and 20 min after the addition of NaOH solution. (c) FLem spectra (λex = 270 nm) and (d) PPem spectra (λex = 230 nm) of C-bSNPs calcined at different temperatures. The magnified spectra in the range of 300–600 nm are shown in the insets.

the fluorescence changes with silica defects as the FL_{em} intensity at 470 nm was noticeably reduced after hydrolysis of silica networks (Fig. 3a). As previously mentioned, this excitation band (~370 nm) is attributed to the 470 nm FL_{em}, resulting from intrinsic silica defects (silylene and dioxasilyrane defect pairs). Because these defects also comprise Si–O bonds, their decomposition was also expected with hydrolysis at alkaline condition, supporting the reduction in FL_{em} centered at 470 nm. However, unlike the fluorescence, the phosphorescence showed no significant change (Fig. 3b). Considering that phosphorescence is preserved under the same conditions, two conclusions can be drawn: (i) the phosphorescence does not originate from organic species, but rather from a defect site within the silica network, and (ii) the defect site contributing to the phosphorescence is expected to be comprised with Si–C bonds, not the Si–O bond-based intrinsic silica defects, since the C-bSNPs only contain Si, O, and C atoms.

The effect of the calcination temperatures on the fluorescence and phosphorescence properties of the C-bSNPs was then investigated. As shown in Fig. 3c, d and S9, the FL_{em} significantly decreased with calcination, while PP_{em} gradually increased upon calcination temperature increase of up to 700 °C. Interestingly, at temperatures above 700 °C, both the fluorescence and phosphorescence states were practically diminished, and the resulting product became identical to pure SNPs, implying that the defect structure was unstable at these calcination temperatures. In addition, the quantum yields for C-bSNPs after calcination at different temperate were correspondingly matched with the PP_{em} (Table S2). Consequently, we inferred that the thermal decomposition of the biphenyl groups embedded in the silica network generated a unique type of defect site comprising a Si–C bond and that this defect essentially initiated the RTP of metal- and fluorophore-free silica NPs.

To investigate the phosphorescence properties with respect to the amount of BTBP precursor, the C-bSNPs were synthesized with different amounts of BTBP (e.g., 0.25, 2, 5, and 10 times higher than that for the C-bSNPs, which is denoted as C-$bSNP_{(0.25)}$, C-$bSNP_{(2)}$, C-$bSNP_{(5)}$, and C-$bSNP_{(10)}$, respectively). The C-bSNPs exhibited the highest phosphorescence intensity among others (Fig. S10), and the intensity decreased with the increased BTBP while slightly reduced at C-$bSNP_{(0.25)}$. To determine the reason behind this observation, TEM imaging revealed that a high BTBP/TEOS ratio resulted in the agglomeration of silica particles (Fig. S11a). Such clustering may hinder phosphorescence carrier recombination, thus substantially reducing the phosphorescence intensity. Interestingly, an onion-like lattice structure, similar to that of biphenylene-bridged organosilica (Fig. S11b), was also observed in the sample before the calcination of C-$bSNP_{(10)}$ [49]. Furthermore, the TEM image of C-$bSNP_{(10)}$ depicts a unique lattice spacing of 0.48 nm after calcination, which is inconsistent with those of organosilica and crystalline silica (Fig. S11c). This unique lattice spacing is likely direct evidence of the structural changes resulting from the thermal decomposition of the biphenyl groups. Therefore, we concluded that after bSNP calcination, the empty site from which the biphenyl group was removed exhibited a unique structure distinct from that of general silica, and phosphorescence-related defects comprising Si–C bonds were generated at this site.

2.4. Computational analysis on the origin of phosphorescence

Experimental findings on the optical properties of C-bSNPs revealed a new absorption band (at ~265 nm) derived by addition of BTBP precursor into TEOS-based Stöber solution to form bSNPs (Fig. 2a). In addition, the XPS results also imply that carbon-related defects in the C-bSNPs might be associated with the newly formed absorption band (Fig. 1g). However, the precise structure of the defects that contribute to this absorption band and their roles in the phosphorescence of the C-bSNPs remain unclear. In this regard, density functional theory (DFT) calculations were further performed to investigate the origin of the phosphorescence in the C-bSNPs. Potential intrinsic defect structures and carbon-related defect structures of SiO_2 were modeled based on previous research (Fig. S12) [50–52], and the simulated absorbance spectra of the defect structures were compared with the experimentally observed absorbance spectra of the C-bSNPs (Fig. S13). The DFT-calculated absorbance spectrum of pure silica (SNPs) was in good agreement with the experimental results (Fig. S13a). For the intrinsic defect structures of silica, such as oxygen deficient center (ODC), peroxy bridge (POL), and silanol (Si–O–H), no specific absorption peaks were observed (Fig. S13b–d). However, for all carbon-related defect structures, an absorption peak appeared near 265 nm (Fig. S13e–h), implying that carbon defect formation owing to the introduction of BTBP as a precursor can be the phosphorescence origin of C-bSNPs.

We then investigated the phosphorescence mechanism of C-bSNPs using DFT calculations. For phosphorescence to occur, the luminescence of a substance commences with electron–hole pair formation through the absorption of incident light (route (1) in Fig. 4a), followed by energy release in the form of light or heat. When the photoexcited electron is rapidly relaxed from excited state (ES) to ground state (GS), light emission occurs (route (2) in Fig. 4a). However, the photoluminescence mechanism can be altered by the formation of defect-induced mid-gap trap states because excited electrons can be captured by these trap states during relaxation. There are two possible scenarios in this context. The first scenario is that the captured electrons may be thermally activated and de-captured to the conduction band, potentially causing thermally activated delayed fluorescence (route (3) in Fig. 4a) [53], but such fluorescence was not observed in our system (Fig. S6d). It means that the de-captured electrons might be relaxed to the trap states or followed non-radiative recombination. Therefore, both recombination and capture processes might be possible for phosphorescence in C-bSNPs, resulting in phosphorescence with a longer wavelength than that of fluorescence (route (4) in Fig. 4a) [54–56]. Accordingly, we investigated the band structures of the promising carbon-related defect structures above (Fig. S13e–h), and the DFT analysis supports that carbon defects introduce new trap states with two transition levels (Fig. 4c–e) compared with the band structure of pure SiO_2 (Fig. 4b). The transition levels in interstitial carbon defect (2.30 eV), C–C defect (2.37 eV), and OC_2O, (2.65 eV) are in good agreement with the experimentally observed emission peak at 470 nm (2.64 eV) (Fig. 2c). Furthermore, the electronic charge densities of the trap states revealed that two transition levels are associated with carbon defects (Fig. S13i–l). Finally, the formation of trap states induced by carbon defects led to the phosphorescence of C-bSNPs.

2.5. Biofunctionalization and in vitro cancer targeting

The C-bSNPs can be readily utilized as biomedical imaging probes because of their uniform morphology, facile surface chemistry, and distinct optical properties. To demonstrate their potential for imaging-guided cancer diagnostics, water-dispersibility and tumor-targeting capability were enhanced by surface functionalization of C-bSNPs. Amine functionalization with 3-aminopropyltriethoxysilane (APTES), followed by carboxylation with succinic anhydride, allows the further modification with a tumor-targeting peptide while retaining the phosphorescence in an aqueous environment (Fig. 5a). Among the various tumor-targeting moieties such as peptides, aptamers, and antibodies, we used a prototypic RPARPAR peptide which specifically recognizes neuropilin-1 (NRP-1) receptor, followed by intracellular uptake through receptor-mediated endocytosis [57–60]. NRP-1 is a multifunctional ligand involved in the signal transduction of various endogenous cytokines and is highly expressed on various tumor cell surfaces that can be targeted by C-end rule (CendR) peptides [61].

The RPARPAR peptide-functionalized C-bSNPs (pep-C-bSNPs) was prepared using molecular conjugation between the carboxylic acid groups on C-bSNPs and the N-terminal aminohexanoic acid of the peptide via a conventional EDC/NHS coupling reaction (Fig. 5a). Next, specific binding affinity of pep-C-bSNPs to SW-480 cells, an NRP-1-positive human colorectal cancer cell line, was observed through

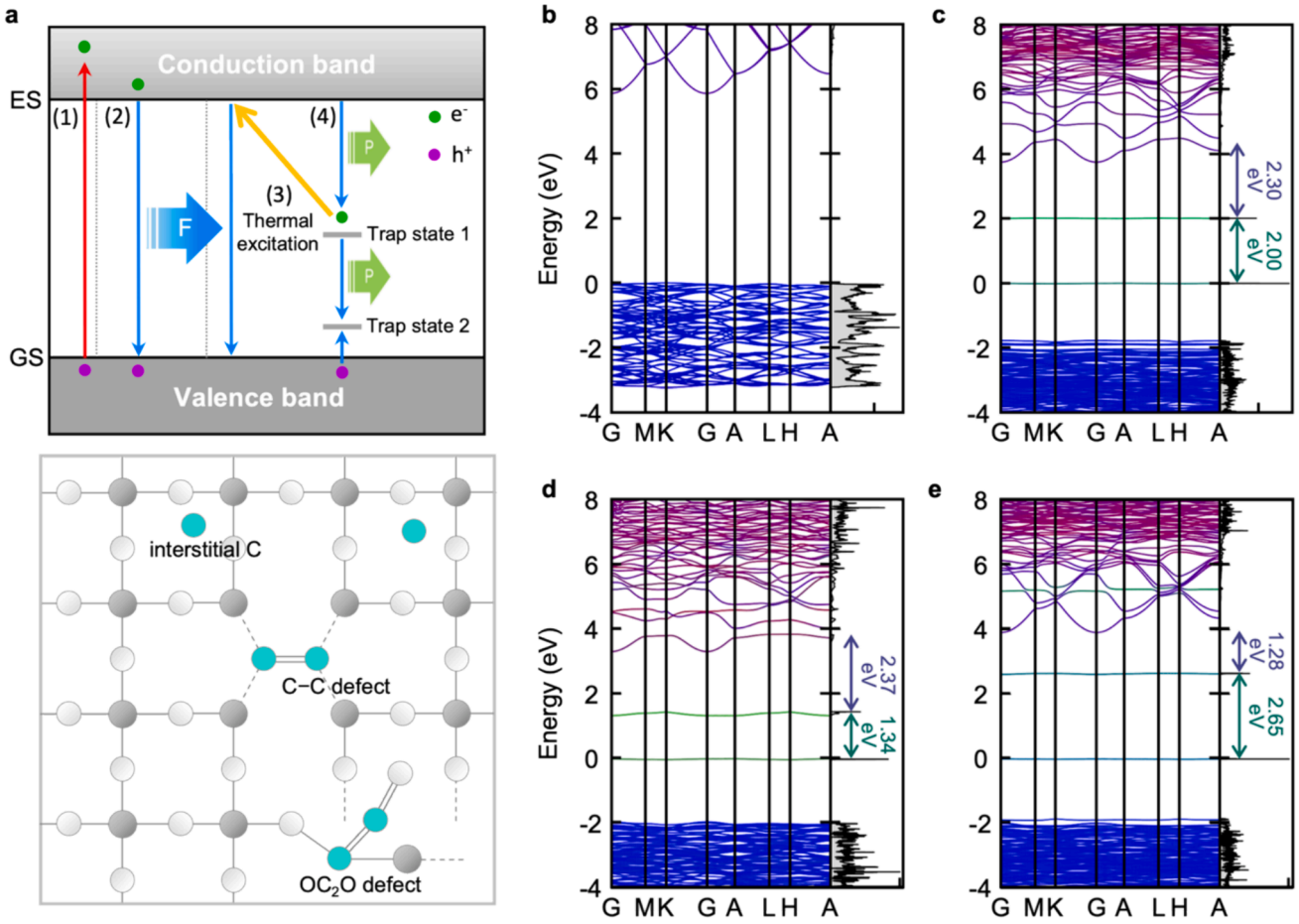

Fig. 4. Theoretical phosphorescence mechanism of C-bSNPs obtained via DFT calculations. (a) Schematic illustration of the band structure including the photoluminescence mechanism: (1) photoexcitation of electrons by incident light; (2) relaxation of excited electrons from excited state (ES) to ground state (GS) (Fluorescence, F); (3) thermal excitation and delayed relaxation; or (4) relaxation through the trap states of excited electrons (phosphorescence, P). e^- and h^+ indicate electron and hole, respectively. DFT-calculated band structure and density of states of (b) pure SiO_2, (c) interstitial carbon defect, (d) C–C defect, and (e) OC_2O defect structures.

confocal microscopy, whereas the C-bSNPs lacking RPARPAR peptide functionalization exhibited negligible cellular uptake (Fig. 5b). In addition, the reduced uptake of pep-C-bSNPs through NRP-1 receptor pre-blocking by treatment with free RPARPAR peptides for 30 min prior to pep-C-bSNP introduction to SW-480 cells further supported the hypothesis that the RPARPAR peptide leads to targeted pep-C-bSNP delivery to SW-480 cells (Fig. S14). In addition, negligible cytotoxicity of both C-bSNPs and pep-C-bSNPs at elevated concentrations of up to 200 μm/mL was verified, despite biphenyl doping and defect sites, in accordance with the biocompatible characteristics of typical SNPs (Fig. S15). Comparing to other organic phosphorescent probes such as 9,9′-(6-iodophenoxy-1,3,5-triazine-2,4-diyl)bis(9H-carbazole) and cyanine dye-based bioorganic nanoparticles, the C-bSNPs showed remarkable biocompatibility as in vivo imaging probe [62–66]. Therefore, the silica nanoparticles were supposed to maintain the intrinsic non-toxic biocompatibility even after doping and calcination process.

2.6. *Time-gated afterglow phosphorescence imaging for in vivo cancer diagnostics*

By employing the cancer-targeting luminescent probe, one can facilitate imaging-guided cancer diagnostics or therapeutics as high accumulation at a suspected tumorous tissue is realized with the targeted imaging probe. However, tissue autofluorescence is one of the most critical challenges in fluorescence-based bioimaging systems because the intrinsic biological components, such as mitochondria, lysosomes, and lipids, comprise endogenous fluorophores that typically absorb light and emit substantial tissue autofluorescence, thereby reducing the visibility of exogenous fluorescent probes. Time-gated imaging is an alternative method for visualizing the emission signals of exogenous probes by capturing the emissive light at a delay time after excitation rather than using continuous-wave excitation [67]. Long-lived afterglow signals enable late time gating to eliminate background noise and interference. In this study, both C-bSNPs and pep-C-bSNPs demonstrated concentration-dependent signal intensity in time-gated afterglow imaging (Fig. 6a). In particular, the phosphorescence characteristics of the two NPs remained comparable even after peptide conjugation. Considering the sufficiently long phosphorescence lifetime of C-bSNPs compared with the nanosecond-scale lifetime of tissue autofluorescence, the persistent emission from C-bSNPs was well differentiated in the time domain from signals associated with endogenous fluorophores and tissue autofluorescence using time-gated afterglow imaging. Delayed afterglow images acquired 10 s after excitation showed strong evidence of long-lived phosphorescence signals, whereas the autofluorescence of background tissue completely disappeared owing to its shorter lifetime (<approximately 10 ns) in mice (Fig. 6b). In contrast, conventional fluorescence imaging performed under continuous-wave excitation exhibited emission signals indistinguishable from the substantial tissue autofluorescence.

Time-gated afterglow phosphorescence imaging of human colorectal cancer xenografts was then demonstrated in a mouse model via intratumoral injections of C-bSNPs (Fig. 6c). The afterglow phosphorescence

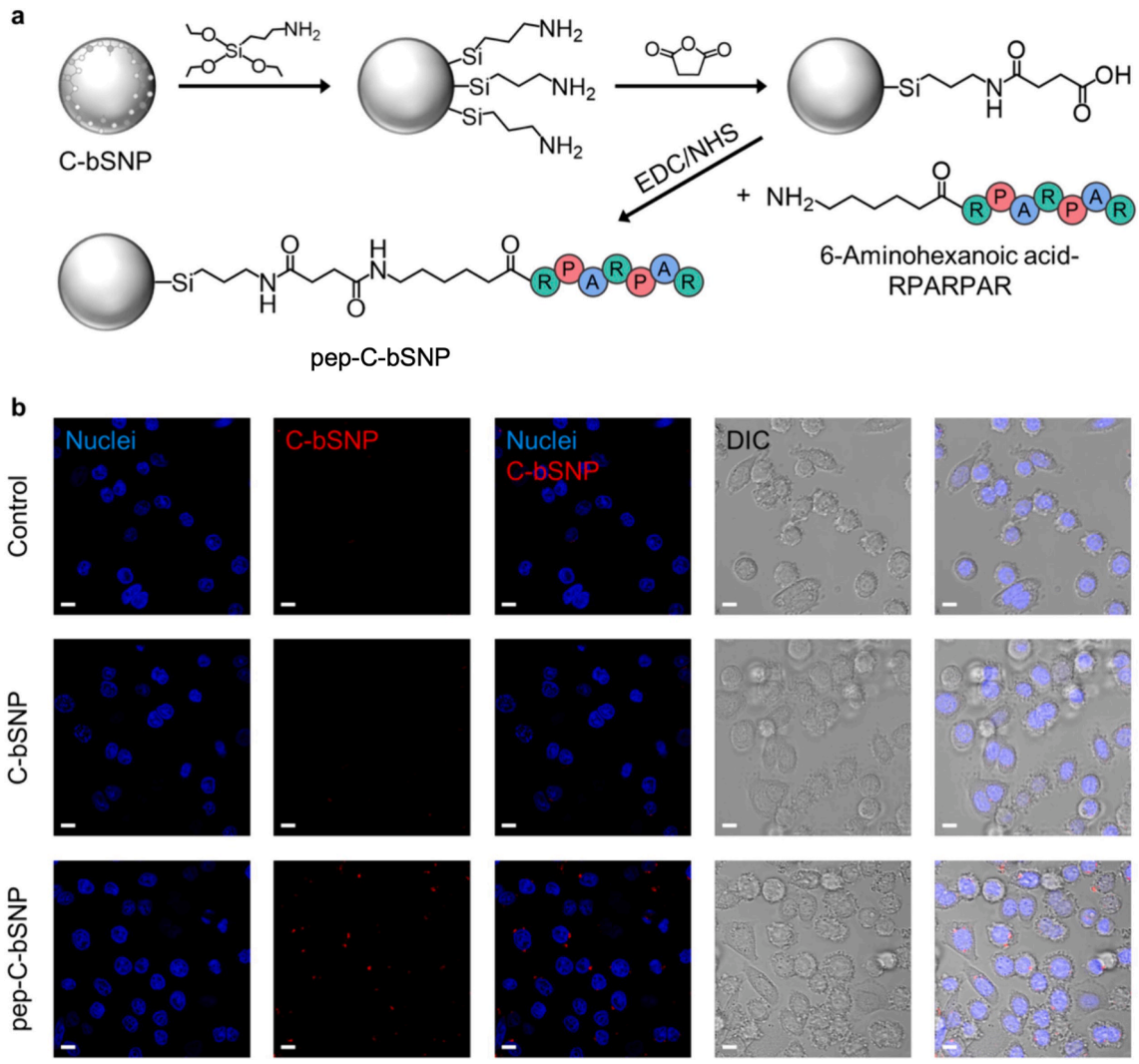

Fig. 5. In vitro cancer cell targeting with pep-C-bSNPs. (a) Schematics of pep-C-bSNPs. (b) Confocal laser scanning microscopy images of SW-480 cells treated for 4 h with medium (control), C-bSNPs, and pep-C-bSNPs (20 μg/mL). Scale bars: 10 μm.

of C-bSNPs was readily displayed at the tumor site with a conventional in vivo imaging system (IVIS) in the luminescence mode following UV light irradiation (λ_{ex} = 365 nm). In addition, the afterglow phosphorescence signals exhibited a delay-time-dependent intensity (Fig. 6d). Long-lived phosphorescence of C-bSNPs was acquired up to 40 s after switching off the light, which was highly beneficial in eliminating the tissue autofluorescence in the time-gated imaging system, and this step can be readily adopted when using conventional fluorescence imaging/optical tomography instruments. Although the intensity of UV excitation light diminishes significantly due to absorption by the tissue beyond a few millimeters, the present autofluorescence-free bioimaging eliminates unavoidable background noise in fluorescence-based in vivo optical imaging. Therefore, the RTP-based in vivo bioimaging can be adopted to distinguish the biological components of interest at least underneath the skin and is able to obtain clear visualization despite the short penetration depth of UV excitation and blue emission. Time-gated afterglow imaging of the tumor tissues further confirmed the presence of C-bSNPs in the tumor and demonstrated the effectiveness of time-gated afterglow imaging of C-bSNPs in ex vivo tissues (Fig. 6e). Although the short penetration depth and potential toxicity of UV light irradiation might limit the use of C-bSNPs as an imaging prove, the time-gated imaging provides a means of highly luminescent visualization as it only requires a very short exposure time (<10 s) while eliminating noisy tissue autofluorescence.

Finally, potential cancer diagnostics using the time-gated afterglow imaging and pep-C-bSNPs was assessed using intravenously injected circulating C-bSNPs as a diagnostic imaging probe. Systemic administration of pep-C-bSNPs revealed gradual increase in luminescence signal corresponding to the timely accumulation at the tumor site, whereas a negligible signal was detected at bare C-bSNPs administrated mice, through time-gated afterglow imaging of a human colorectal cancer xenograft mouse model (Fig. 6f). Notably, intravenously injected NPs passively accumulate in tumor tissues owing to the enhanced permeability and retention (EPR) effect. In this study, the capability of C-bSNPs to target tumors was negligible under passive accumulation via the EPR effect, whereas a significant amount of pep-C-bSNPs was observed with the active targeting strategy. Ex vivo tumor tissue imaging clearly demonstrated the superior targeting capability of the pep-C-bSNPs and corresponded to the results obtained from the time-gated afterglow imaging of live tumor-bearing mice (Fig. 6g and Fig. S16). Moreover, we also found non-specific accumulation of both NPs at other major organs including liver, spleen, and lung while negligible signals were detected from in vivo live imaging due to the limited penetration depth of light. Despite the significant targeting capability of pep-C-bSNPs (>1.5 %) compared to bare C-bSNPs (<0.4 %), majority of NPs were still passively accumulated in the liver and spleen rather than the tumor. However, the imaging-based cancer diagnosis utilizing the RTP and afterglow imaging system is potentially useful to detect very early

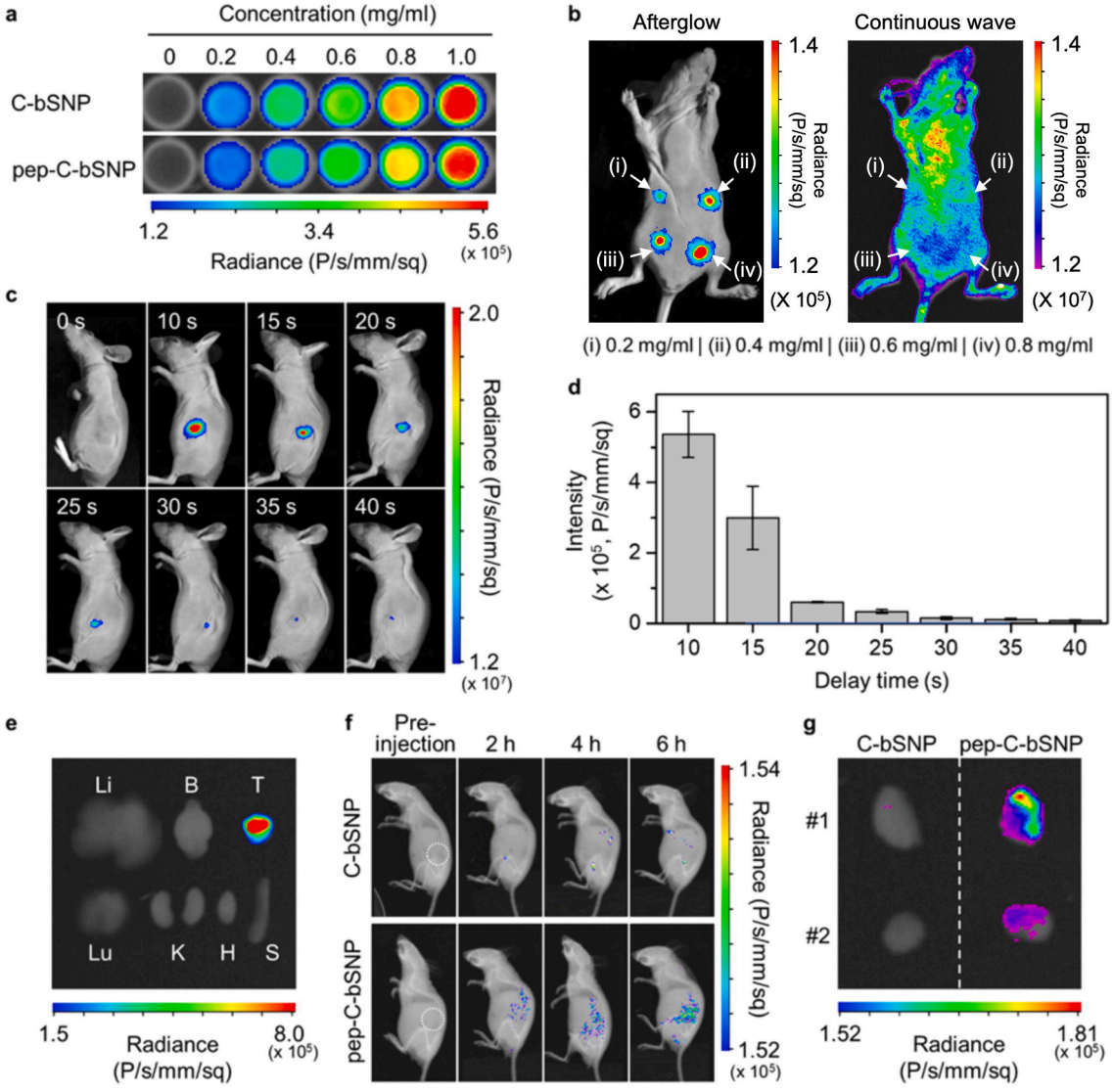

Fig. 6. Validation of the potential of C-bSNPs as a nontoxic, effective imaging probe for cancer diagnostics through time-gated afterglow imaging. (a) Time-gated afterglow images of C-bSNPs and pep-C-bSNPs obtained using the IVIS (λex = 365 nm; delay time = 10 s). (b) Time-gated afterglow (λex = 365 nm; no emission filter; delay time = 10 s) and fluorescence under continuous-wave excitation (λex = 410 nm; λem = 535 nm) images of mouse after subcutaneous injection of C-bSNPs (100 μL), respectively. The afterglow image shows clear evidence of the long-lived phosphorescence of C-bSNPs, whereas the substantial tissue autofluorescence interferes with the luminescent signal of C-bSNPs, resulting in an indiscriminate signal-to-noise ratio for C-bSNP detection. (c) In vivo live time-gated afterglow images of tumor-bearing mice with the intratumoral injection of C-bSNPs (8 mg/mL, 50 μL in PBS) with different delay times as indicated (λex = 365 nm; no emission filter), and (d) corresponding afterglow intensity (±standard deviation) of C-bSNPs at the tumor site as a function of the delay time (n = 3). (e) Ex vivo afterglow image of major organs harvested 5 h after intratumoral injection, indicating tissue autofluorescence-free detection of C-bSNPs at the tumor. (Li: liver; B: brain; T: tumor; Lu: lung; K: kidney; H: heart; S: spleen.) (f) In vivo live time-gated afterglow images (λex = 365 nm; delay time = 10 s) of tumor-bearing mice with intravenous injection (20 mg/mL, 100 μL in PBS) of C-bSNPs or pep-C-bSNPs. Note that the dotted white circles indicate the tumor region. (g) Ex vivo afterglow image of tumors harvested from two mice for each group at 8 h post injection.

stage of cancers by observing small extents of targeted NPs in vivo.

Because of the limited tissue penetration depth of UV excitation and blue emission, the afterglow time-gated imaging is only eligible to visualize subcutaneous or ex vivo tissues rather than deep tissue live imaging. Nevertheless, autofluorescence-free afterglow imaging using C-bSNPs can be further extended to study in vivo cancer targeting, accumulation, and biodegradation at deep tissue level with appropriate imaging settings such as intravital or endoscopic imaging systems, where superior signal-to-noise ratio is required by eliminating substantial tissue autofluorescence [68,69]. In addition, UV irradiation employed in the present study exhibits negligible DNA damage, as native DNA poorly absorbs the light at this range (315–400 nm) [70]. In addition, due to the high QY (~26.51 %), the excitation light irradiation can be minimized to avoid any adverse effect such as DNA damage and mutation caused by UV exposure. In fact, the UV excitation power (~1.6 mW/cm^2) was less than 10-fold lower than the maximum power exposure (MPE) permissible for skin irradiation (18 mW/cm^2) [71]. Despite the potential limitations using UV light as an excitation light source, exceptionally long-lived phosphorescence of C-bSNPs in room temperature is promising to clearly visualize the imaging probe at least near the skin and(or) superficial tissues without concerns of cytotoxicity, comparable to literatures [72–75].

Further validation revealed no obvious cytotoxicity of C-bSNPs in the histological evaluation of major organs 7 d post injection. After staining with hematoxylin and eosin (H&E), no significant tissue damage or inflammation was observed in either C-bSNP- or pep-C-bSNP −injected mice compared with the saline group (Fig. S17). As we found no evidence of residual silica in histological analysis in major organs, the

nanoparticles were supposed to be cleared and completely removed from the tissues. Overall, the results indicate that pep-C-bSNPs are a nontoxic, effective imaging probe for diagnosing tumors through noninvasive time-gated afterglow imaging. Compared to conventional organic dyes, such as FITC and Cy5.5 for bioimaging, C-bSNPs have superior features to eliminate the tissue autofluorescence background while exhibiting high quantum yield. By using near-infrared-emitting dyes such as Cy5.5, the tissue autofluorescence could be reduced. However, the short circulation half-life due to rapid renal clearance leads to less potency for specific targeting in vivo (Fig. S18). Moreover, the colloidal stability of C-bSNPs were acceptable to be administrated in high concentration in PBS (20 mg/mL) as it reaches a stable dispersion of lower concentration (1.25 mg/mL) in the blood stream with an injection rate of 6.6 μL/s. Following the intravenous administration, the NPs were supposed to distribute evenly throughout the body while maintaining colloidal stability, indicating no significant concern regarding aggregation or dispersity in vivo (Fig. S19).

3. Conclusion

In this study, we report defect-engineered silica NPs as a metal- and organic-fluorophore-free novel RTP material. bSNPs are synthesized via modified Stöber method with TEOS and BTBP as co-precursors, and carbon-related defects in the silica network are generated by controlled calcination. Carbon-related defects are the origin of long-lived phosphorescence via intersystem crossing. Under excitation light irradiation, the calcined bSNPs (C-bSNPs) emit bright green (480 nm) RTP lasting over 10 s and is visible to the naked eye. Considering the results of the chemical analyses and theoretical calculations, the thermal decomposition of the biphenyl groups embedded into the silica network is inferred to have generated multiple defect structures containing Si–C bonds. These carbon-related defect structures, including interstitial C, C–C, and OC_2O defect structures, generate the sub-bandgap trap states that permit triplet excitons. The rigid silica network effectively prevents the quenching of triplet excitons by oxygen and moisture, thereby facilitating the production of C-bSNPs with long-lived RTP. In addition, RTP is stably retained in an aqueous environment even after tumor-targeting peptide conjugation. Finally, we show that potential cancer diagnostics using the time-gated afterglow imaging system and tumor-homing RPARPAR peptide-functionalized C-bSNPs (pep-C-bSNPs). Tissue autofluorescence-free bioimaging is achieved as a beneficial tool for high-contrast imaging-based cancer diagnostics, which is useful by adopting long-lived phosphorescence lasting over 30 s. This work not only paves the way for the design and preparation of sustainable and reproducible RTP materials but also provides guidance for their biological applications and translational medicine. We also believe that our theoretical approaches hold potential for screening defect structures, facilitating the design of advanced RTP materials.

4. Materials and methods

4.1. Materials

TEOS (99.0 %), BTBP (90 %), (3-aminopropyl)triethoxysilane (99 %), succinic anhydride (≥99 %), ammonium hydroxide solution (28 % NH_3 in H_2O, ≥99.99 %), and N,N-dimethylformamide (99.8 %) were purchased from Sigma-Aldrich (St. Louis, MO), while ethanol (95 %) was obtained from Duksan Pure Chemicals (Ansan, Korea). The RPARPAR peptide, with an aminohexanoic acid linker on the N-terminal group, was synthesized by Peptron (Daejeon, Korea). N-Hydroxysulfosuccinimide sodium salt (sulfo-NHS) and N-(3-dimethylaminopropyl)-N-ethylcarbodiimide hydrochloride (EDC) were procured from Sigma-Aldrich. All the solutions were prepared using triple-distilled water, and all the chemicals were used without further purification.

4.2. Synthesis of silica nanoparticles (SNPs), biphenyl-doped SNPs (bSNPs), C-SNPs, and calcined bSNPs (C-bSNPs)

Ethanol (100 mL), ammonium hydroxide solution (6 mL, 28 %), and distilled water (2 mL) were mixed in a 250 mL glass beaker and stirred for 30 min at room temperature. Next, 1.2 mL of TEOS was added to the mixed solution, and the solution was vigorously stirred at room temperature for 24 h to obtain SNPs. For bSNPs, 8.4 μL of BTBP was added to the solution with TEOS. Following the reaction, the synthesized SNPs and bSNPs were centrifuged at 6000 rpm for 20 min and the supernatants were decanted, purified with ethanol three times by centrifugation, and subsequently dried in a vacuum oven at 60 °C. The refined SNPs and bSNPs were annealed at 500 °C for 8 h in a muffle furnace in air to produce C-SNPs and C-bSNPs, respectively.

4.3. Controlling synthetic parameters related with optical properties

First, 100 mg of C-bSNPs was dissolved in 10 mL of water; subsequently, 2 M NaOH solution (10 mL) was added dropwise. The mixture was heated to 100 °C and stirred for 20 min. The translucent solution turned transparent as the reaction progressed. Following the reaction, the solution was centrifuged at 6000 rpm for 10 min, washed three times with ethanol, and dried at 60 °C overnight. The C-bSNPs were considered to decompose successfully when no particulate settlement was observed for 1 h. To investigate the effect of the calcination temperature on the fluorescence and phosphorescence properties of C-bSNPs, bSNPs were prepared using the same synthesis method and calcined at different temperatures (300, 400, 600, 700, and 800 °C) for the same duration (8 h). To investigate the optical properties considering the precursor amount, a series of bSNPs with different concentrations of BTBP precursor were prepared. BTBP amounts of 3.36, 16.8, 33.6, and 84 μL were added along with TEOS, and the resultant materials were calcined at 500 °C for 8 h using a muffle furnace to yield C-$bSNP_{(0.5)}$, C-$bSNP_{(2)}$, C-$bSNP_{(5)}$, and C-$bSNP_{(10)}$, respectively (Fig. S20). Note that the C-bSNPs calcined at 500 °C were chosen for in vitro and in vivo demonstration because the phosphorescence intensity at 360 nm excitation wavelength, corresponding to the UV irradiation wavelengths used for afterglow imaging, does not significantly increase beyond 500 °C (Fig. S21). Considering practical uses with cost-effective and scalable synthesis process, C-bSNPs calcined at 500 °C were also feasible for further bioimaging applications.

4.4. Characterization

For the TEM observation, first, 1 mg of the sample was dispersed in 1 mL of methanol by sonication and then dropped onto a lacey carbon grid. TEM was performed using a JEM-2100F instrument (at an accelerating voltage of 200 kV) equipped with a Cs corrector. ATR-FTIR spectroscopy was performed using a Nicolet iS50 FTIR spectrometer (Thermo Scientific). Powder XRD was performed using a D8 Advance X-ray diffractometer (TRIO/TWIN, Bruker) with Cu Kα radiation at 40 kV and 40 mA. XPS was performed using a Nexsa (Thermo Fisher) instrument with an Al Kα X-ray source (1486.6 eV). GC/MS was performed on an Agilent HP 7890 gas chromatograph combined with combined with an Agilent 5977E mass selective detector. UV–Vis absorption spectroscopy was performed on samples in an aqueous solution (0.15 mg/mL) using a Scinco S3100 UV–Vis spectrometer equipped with Hellma Analytics QS-grade quartz cuvettes (111-QS). Photoluminescence (fluorescence/phosphorescence) spectroscopy was performed on a Jasco FP-8500 fluorometer with samples in the powder form. The absolute quantum yield was measured using a Jasco ILF-835 integrating sphere (Fig. S22). The sample, in powder form, was ground with a mortar, transferred into a 3-mm-thick quartz cuvette, and placed on the rack inside the integrating sphere. After pre-exposing the sample to 270 nm excitation for 5 min, absorptance and PL emission were measured. The results were analyzed using Jasco Spectra Manager II Version 2 software

(Table S2). The photoluminescence decay times were measured using a Fluorolog (3-series Horiba) instrument with a time-correlated single-photon counter.

4.5. Computational analysis

DFT calculations were performed using the Vienna ab initio Simulation Package (VASP) [76,77]. Exchange-correlation energies were treated using the Perdew–Burke–Ernzerhof functional based on the generalized gradient approximation [78]. A plane-wave expansion with a cutoff energy of 400 eV was applied with $3 \times 3 \times 2$ Monkhorst–Pack k-point sampling of the Brillouin zone for $2 \times 2 \times 2$ supercells of pure and defective α-quartz SiO_2 [79]. The geometries were relaxed using a conjugate gradient algorithm until the forces on all unconstrained atoms dropped below 0.03 eV/Å. The convergence criterion was set at 10^{-4} eV. All the optimized structures were visualized by VESTA [80]. The absorption spectra were obtained using the frequency-dependent complex dielectric function [81,82].

4.6. Biofunctionalization of C-bSNPs

COOH functionalization for endowing C-bSNPs with both water solubility and peptide conjugation was performed through sequential surface chemistry according to a literature [83,84]. C-bSNPs (100 mg) were dispersed in ethanol (100 mL) through sonication, and then aqueous NaOH (6 mL, 28 %) and distilled water (2 mL) were added to the solution. After the solution was stirred for 30 min, 0.3 mL of APTES was added, and the reaction solution was further stirred for 24 h. The resulting NH_2-functionalized C-bSNPs were rinsed three times with N,N-dimethylformamide and water, respectively. The C-bSNP powder was then dispersed in 20 mL of DMF, and a succinic anhydride solution (0.1 M, 20 mL) was subsequently added dropwise, followed by stirring for 24 h at room temperature. After washing three times with ethanol, COOH-functionalized C-bSNPs were obtained. To conjugate the tumor-homing peptide, an aliquot (1 mL) of the COOH-functionalized C-bSNPs (1 mg/mL in PBS) was sequentially treated with 5 mg sulfo-NHS, 2.8 μL of EDC, and 45 μL of RPARPAR peptide (1 mg/ml in deionized water) under vigorous agitation (1000 rpm) at room temperature for 6 h. The peptide-conjugated C-bSNPs (pep-C-bSNPs) were purified using centrifugation and washed three times with PBS. Finally, the stock solution of pep-C-bSNP was stored in the dark at 4 °C until use.

4.7. In vitro cellular uptake

Human colorectal cancer cells (SW-480, ATCC, USA) were seeded onto Nunc eight-well chambered coverglass (Thermo Scientific) at a density of 2×10^4 cells/well and allowed to grow at a temperature of 37 °C with 5 % CO_2 for 24 h. The culture medium was replaced with RPMI 1640 medium (Gibco) containing C-bSNPs or pep-C-bSNPs at a concentration of 20 μg/mL. After 4 h of incubation, the cells were washed with PBS and stained with SYTO deep red nucleic acid (Invitrogen) to visualize the nuclei. Confocal laser scanning microscopy (ZEISS LSM780) was employed for the cellular uptake analysis using ZEN 3.4 (blue edition) software.

4.8. In vitro viability

To evaluate the in vitro cytotoxicity of the synthesized nanoparticles, SW-480 cells were treated with either C-bSNPs or pep-C-bSNPs at elevated concentrations. The cells were seeded in a 96-well plate at 5×10^4 cells per well and incubated for 12 h in a 37 °C, 5 % CO_2 incubator. Subsequently, the cell culture medium was replaced with 100 μL of fresh medium (no phenol red) containing C-bSNPs or pep-C-bSNPs at various concentrations (0.2, 0.4, 0.6, 0.8, and 1.0 mg/mL) and incubated for 6 h. The cell viability was determined by CCK-8 assay, where 5 μL of CCK-8 solution was added to each well, and the cells were further incubated for 30 min. The absorbance at 450 nm was measured using a microplate reader, and the relative cell viability was quantitatively analyzed through comparison with nontreated cells.

4.9. Experimental animals and xenograft models

Female BALB/c nude mice (six weeks old) were purchased from Orient Bio (Korea) and treated in accordance with the guidelines of the Institutional Animal Care and Use Committee (IACUC) at Ulsan National Institute of Science and Technology (#UNISTIACUC-22–28). For the in vivo xenograft mouse model, SW-480 cells (5×10^6 cells) were diluted in 60 μL of Hank's balanced salt solution and immersed in 60 μL of Matrigel (BD Bioscience), and subcutaneously injected into the right flank of the mice.

4.10. Time-gated afterglow phosphorescence imaging

For the initial demonstration of afterglow imaging in vivo, C-bSNPs (100 μL) were subcutaneously injected into the abdomen of living mice at various concentrations (0.2, 0.4, 0.6, and 0.8 mg/mL). Time-gated afterglow images were acquired using the IVIS in the bioluminescence mode promptly after light irradiation by a handheld UV lamp (365 nm). For intratumoral injection, C-bSNPs (50 μL, 8 mg/mL) were directly injected into the tumorous region of the mice of SW-480 bearing xenografts. In the time-gated imaging, afterglow signals were acquired using the IVIS in various time domain. The delay time was manually controlled by adjusting the start time of the IVIS acquisition. For the systemic administration of C-bSNPs and imaging-guided cancer diagnosis, both C-bSNPs and pep-C-bSNPs (100 μL, 20 mg/mL) were intravenously injected through the tail vein of the SW-480 xenograft mouse model. Time-gated afterglow images were acquired using the IVIS at a delay time of 10 s.

4.11. H&E staining

Major organs of the mice in three groups were collected and fixed with 10 % neutral buffered formalin. The organs were then embedded in paraffin and sectioned at 6 μm thickness, and then stained with hematoxylin and eosin staining (H&E). Furthermore, the tumor tissues were collected for H&E staining to evaluate the histopathological changes. The images of these sections were observed using a microscope.

CRediT authorship contribution statement

Heemin Chang: Writing – original draft, Methodology, Investigation, Data curation, Conceptualization. **Yoonsang Park:** Writing – original draft, Methodology, Investigation, Formal analysis, Data curation, Conceptualization. **Kyunghwan Kim:** Writing – original draft, Validation, Methodology, Investigation, Data curation. **Chaewon Han:** Formal analysis, Data curation. **Yeongjun Yoon:** Validation, Investigation, Formal analysis. **Woojung Yoo:** Methodology, Formal analysis, Data curation. **Jounghyun Yoo:** Validation, Investigation, Conceptualization. **Dajin Lee:** Validation, Formal analysis. **Hyunho Han:** Validation, Investigation. **Kyeounghak Kim:** Writing – review & editing, Writing – original draft, Supervision, Project administration, Investigation, Funding acquisition, Conceptualization. **Jinmyoung Joo:** Writing – review & editing, Writing – original draft, Supervision, Project administration, Investigation, Funding acquisition, Conceptualization. **Woosung Kwon:** Writing – review & editing, Writing – original draft, Supervision, Project administration, Investigation, Funding acquisition, Conceptualization.

Declaration of competing interest

The authors declare that they have no known competing financial interests or personal relationships that could have appeared to influence

the work reported in this paper.

Data availability

Data will be made available on request.

Acknowledgements

This research was primarily supported by the Basic Science Research Programs (NRF-2022R1A2C4002403 and RS-2023-00209822) of the National Research Foundation of Korea. This research was also supported in part by a grant of the Korea Dementia Research Project through the Korea Dementia Research Center (KDRC), funded by the Ministry of Health & Welfare and Ministry of Science and ICT (RS-2020-KH106391) and by the Korean Fund for Regenerative Medicine (KFRM) funded by the Ministry of Science and ICT and the Ministry of Health & Welfare (22A0102L1-11). H.H. acknowledges the support of the Yonsei University College of Medicine Faculty Research Grant (6-2021-0116). Kyeoung.K. acknowledges the support of the Engineering Research Center of Excellence Program (NRF-2022R1A5A1033719) of the National Research Foundation of Korea. J.J. acknowledges the POSCO Science Fellowship of the POSCO TJ Park Foundation and the Future-leading Project Research Fund (1.240006.01) of UNIST. This work was supported in part by NSF through the UC San Diego Materials Research Science and Engineering Center (UCSD MRSEC) DMR-2011924.

Appendix A. Supplementary data

Supplementary data to this article can be found online at https://doi.org/10.1016/j.cej.2024.152529.

References

[1] E.M.S. Stennett, M.A. Ciuba, M. Levitus, Photophysical processes in single molecule organic fluorescent probes, Chem. Soc. Rev. 43 (4) (2014) 1057–1075.
[2] M. Liu, N. Yazdani, M. Yarema, M. Jansen, V. Wood, E.H. Sargent, Colloidal quantum dot electronics, Nat. Electron. 4 (8) (2021) 548–558.
[3] T.J. Penfold, E. Gindensperger, C. Daniel, C.M. Marian, Spin-vibronic mechanism for intersystem crossing, Chem. Rev. 118 (15) (2018) 6975–7025.
[4] M.K. Nazeeruddin, R. Humphry-Baker, D. Berner, S. Rivier, L. Zuppiroli, M. Graetzel, Highly phosphorescence iridium complexes and their application in organic light-emitting devices, J. Am. Chem. Soc. 125 (29) (2003) 8790–8797.
[5] T. Zheng, W.C.H. Choy, High efficiency blue organic LEDs achieved by an integrated fluorescence-interlayer-phosphorescence emission architecture, Adv. Funct. Mater. 20 (4) (2010) 648–655.
[6] M. Louis, H. Thomas, M. Gmelch, A. Haft, F. Fries, S. Reineke, Blue-light-absorbing thin film showing ultralong room-temperature phosphorescence, Adv. Mater. 31 (12) (2019) 1807887.
[7] D. Li, M. Li, W. Li, W. Li, Z. Chen, X. Peng, D. Liu, G.-X. Yang, S. Jiang, Y. Gan, Z. Yang, K. Liu, S.-J. Su, Spiral donor-based host materials for highly efficient blue thermally activated delayed fluorescence OLEDs, Chem. Eng. J. 458 (2023) 141416.
[8] X. Wang, H. Ma, M. Gu, C. Lin, N. Gan, Z. Xie, H. Wang, L. Bian, L. Fu, S. Cai, Z. Chi, W. Yao, Z. An, H. Shi, W. Huang, Multicolor ultralong organic phosphorescence through alkyl engineering for 4D coding applications, Chem. Mater. 31 (15) (2019) 5584–5591.
[9] Q. Gao, W. Zhang, B. Song, R. Zhang, W. Guo, J. Yuan, Development of a novel lysosome-targeted ruthenium(II) complex for phosphorescence/time-gated luminescence assay of biothiols, Anal. Chem. 89 (8) (2017) 4517–4524.
[10] X. Zhen, Y. Tao, Z. An, P. Chen, C. Xu, R. Chen, W. Huang, K. Pu, Ultralong phosphorescence of water-soluble organic nanoparticles for in vivo afterglow imaging, Adv. Mater. 29 (33) (2017) 1606665.
[11] M. Hembury, C. Chiappini, S. Bertazzo, T.L. Kalber, G.L. Drisko, O. Ogunlade, S. Walker-Samuel, K.S. Krishna, C. Jumeaux, P. Beard, C.S. Kumar, A.E. Porter, M. F. Lythgoe, C. Boissiere, C. Sanchez, M.M. Stevens, Gold-silica quantum rattles for multimodal imaging and therapy, Proc. Natl. Acad. Sci. 112 (7) (2015) 1959–1964.
[12] J. Wang, J.J. Nie, P. Guo, Z. Yan, B. Yu, W. Bu, Rhodium(I) complex-based polymeric nanomicelles in water exhibiting coexistent near-infrared phosphorescence imaging and anticancer activity in vivo, J. Am. Chem. Soc. 142 (6) (2020) 2709–2714.
[13] D. Chen, W. Wang, Q. Zhu, Q. Wang, D. Quan, Y. Zeng, K. Li, Y. Zhou, C. Liu, W. Zhan, Y. Zhan, In vivo real-time monitoring of the development of hypoxia and angiogenesis in cervical cancer, Chem. Eng. J. 473 (2023) 145498.
[14] C.-H. Lin, Y.-Y. Chang, J.-Y. Hung, C.-Y. Lin, Y. Chi, M.-W. Chung, C.-L. Lin, P.-T. Chou, G.-H. Lee, C.-H. Chang, W.-C. Lin, Iridium(III) complexes of a dicyclometalated phosphite tripod ligand: strategy to achieve blue phosphorescence without fluorine substituents and fabrication of OLEDs, Angew. Chem. Int. Ed. 50 (14) (2011) 3182–3186.
[15] Q. Dang, Y. Jiang, J. Wang, J. Wang, Q. Zhang, M. Zhang, S. Luo, Y. Xie, K. Pu, Q. Li, Z. Li, Room-temperature phosphorescence resonance energy transfer for construction of near-infrared afterglow imaging agents, Adv. Mater. 32 (52) (2020) 2006752.
[16] W.H. Green, K.P. Le, J. Grey, T.T. Au, M.J. Sailor, White phosphors from a silicate-carboxylate sol-gel precursor that lack metal activator ions, Science 276 (5320) (1997) 1826–1828.
[17] L. Zhao, T. Ming, H. Chen, L. Gong, J. Chen, J. Wang, Room-temperature metal-activator-free phosphorescence from mesoporous silica, Phys. Chem. Chem. Phys. 13 (6) (2011) 2387–2393.
[18] P. Pander, A. Swist, J. Soloducho, F.B. Dias, Room temperature phosphorescence lifetime and spectrum tuning of substituted thianthrenes, Dyes Pigm. 142 (2017) 315–322.
[19] Z. He, H. Gao, S. Zhang, S. Zheng, Y. Wang, Z. Zhao, D. Ding, B. Yang, Y. Zhang, W. Z. Yuan, Achieving persistent, efficient, and robust room-temperature phosphorescence from pure organics for versatile applications, Adv. Mater. 31 (18) (2019) 1807222.
[20] L. Gu, H. Wu, H. Ma, W. Ye, W. Jia, H. Wang, H. Chen, N. Zhang, D. Wang, C. Qian, Z. An, W. Huang, Y. Zhao, Color-tunable ultralong organic room temperature phosphorescence from a multicomponent copolymer, Nat. Commun. 11 (1) (2020) 944.
[21] J. Wang, Z. Huang, X. Ma, H. Tian, Visible-light-excited room-temperature phosphorescence in water by cucurbit[8]uril-mediated supramolecular assembly, Angew. Chem. Int. Ed. 59 (25) (2020) 9928–9933.
[22] J. Zhi, Q. Zhou, H. Shi, Z. An, W. Huang, Organic Room temperature phosphorescence materials for biomedical applications, Chem. Asian J. 15 (7) (2020) 947–957.
[23] S. Guo, W. Dai, X. Chen, Y. Lei, J. Shi, B. Tong, Z. Cai, Y. Dong, Recent progress in pure organic room temperature phosphorescence of small molecular host-guest systems, ACS Mater. Lett. 3 (4) (2021) 379–397.
[24] X.-K. Ma, Y. Liu, Supramolecular purely organic room-temperature phosphorescence, Acc. Chem. Res. 54 (17) (2021) 3403–3414.
[25] Y. Xu, Y. Zhu, L. Kong, S. Sun, F. Li, F. Tao, L. Wang, G. Li, Efficient ultralong and color-tunable room-temperature phosphorescence from polyacrylamide platform by introducing sulfanilic acid, Chem. Eng. J. 453 (2023) 139753.
[26] J. Yang, X. Zhen, B. Wang, X. Gao, Z. Ren, J. Wang, Y. Xie, J. Li, Q. Peng, K. Pu, Z. Li, The influence of the molecular packing on the room temperature phosphorescence of purely organic luminogens, Nat. Commun. 9 (1) (2018) 840.
[27] Kenry, C. Chen, B. Liu, Enhancing the performance of pure organic room-temperature phosphorescent luminophores, Nat. Commun. 10 (1) (2019) 2111.
[28] Y. Lei, W. Dai, Y. Tian, J. Yang, P. Li, J. Shi, B. Tong, Z. Cai, Y. Dong, Revealing insight into long-lived room-temperature phosphorescence of host-guest systems, J. Phys. Chem. Lett. 10 (20) (2019) 6019–6025.
[29] W. Zhao, Z. He, B.Z. Tang, Room-temperature phosphorescence from organic aggregates, Nat. Rev. Mater. 5 (12) (2020) 869–885.
[30] J. Shi, W. Tao, Y. Zhou, G. Liang, Efficient room-temperature phosphorescence with tunable lifetime through light modulation from flexible polymer films, Chem. Eng. J. 475 (2023) 146178.
[31] D. Lee, O. Bolton, B.C. Kim, J.H. Youk, S. Takayama, J. Kim, Room temperature phosphorescence of metal-free organic materials in amorphous polymer matrices, J. Am. Chem. Soc. 135 (16) (2013) 6325–6329.
[32] M.S. Kwon, D. Lee, S. Seo, J. Jung, J. Kim, Tailoring intermolecular interactions for efficient room-temperature phosphorescence from purely organic materials in amorphous polymer matrices, Angew. Chem. Int. Ed. 53 (42) (2014) 11177–11181.
[33] J. Joseph, A.A. Anappara, Cool white, persistent room-temperature phosphorescence in carbon dots embedded in a silica gel matrix, Phys. Chem. Chem. Phys. 19 (23) (2017) 15137–15144.
[34] S. Tao, S. Lu, Y. Geng, S. Zhu, S.A.T. Redfern, Y. Song, T. Feng, W. Xu, B. Yang, Design of metal-free polymer carbon dots: A new class of room-temperature phosphorescent materials, Angew. Chem. Int. Ed. 57 (9) (2018) 2393–2398.
[35] G. Tang, K. Zhang, T. Feng, S. Tao, M. Han, R. Li, C. Wang, Y. Wang, B. Yang, One-step preparation of silica microspheres with super-stable ultralong room temperature phosphorescence, J. Mater. Chem. C 7 (28) (2019) 8680–8687.
[36] L. Gu, D.J. Hall, Z. Qin, E. Anglin, J. Joo, D.J. Mooney, S.B. Howell, M.J. Sailor, In vivo time-gated fluorescence imaging with biodegradable luminescent porous silicon nanoparticles, Nat. Commun. 4 (1) (2013) 2326.
[37] J. Joo, X. Liu, V.R. Kotamraju, E. Ruoslahti, Y. Nam, M.J. Sailor, Gated luminescence imaging of silicon nanoparticles, ACS Nano 9 (6) (2015) 6233–6241.
[38] Q. Miao, C. Xie, X. Zhen, Y. Lyu, H. Duan, X. Liu, J.V. Jokerst, K. Pu, Molecular afterglow imaging with bright, biodegradable polymer nanoparticles, Nat. Biotechnol. 35 (11) (2017) 1102–1110.
[39] S. Liang, G. Liao, W. Zhu, L. Zhang, Manganese-based hollow nanoplatforms for MR imaging-guided cancer therapies, Biomater. Res. 26 (1) (2022) 32.
[40] L. Xu, K. Zhou, H. Ma, A. Lv, D. Pei, G. Li, Y. Zhang, Z. An, A. Li, G. He, Ultralong organic phosphorescent nanocrystals with long-lived triplet excited states for afterglow imaging and photodynamic therapy, ACS Appl. Mater. Interfaces 12 (16) (2020) 18385–18394.
[41] M.J. Byun, J. Lim, S.-N. Kim, D.-H. Park, T.-H. Kim, W. Park, C.G. Park, Advances in nanoparticles for effective delivery of RNA therapeutics, BioChip J. 16 (2) (2022) 128–145.
[42] J. Dai, J. Li, Y. Zhang, Q. Wen, Y. Lu, Y. Fan, F. Zeng, Z. Qian, Y. Zhang, S. Fu, GM-CSF augmented the photothermal immunotherapeutic outcome of self-driving gold nanoparticles against a mouse CT-26 colon tumor model, Biomater. Res. 27 (1) (2023) 105.

[43] Y. Jin, D. Kim, H. Roh, S. Kim, S. Hussain, J. Kang, C.G. Pack, J.K. Kim, S.J. Myung, E. Ruoslahti, M.J. Sailor, S.C. Kim, J. Joo, Tracking the fate of porous silicon nanoparticles delivering a peptide payload by intrinsic photoluminescence lifetime, Adv. Mater. 30 (35) (2018) e1802878.

[44] S. Mukherjee, P. Thilagar, Recent advances in purely organic phosphorescent materials, Chem. Commun. 51 (55) (2015) 10988–11003.

[45] S.A. Yang, S. Choi, S.M. Jeon, J. Yu, Silica nanoparticle stability in biological media revisited, Sci. Rep. 8 (1) (2018) 185.

[46] L. Cursi, S. Vercellino, M.M. McCafferty, E. Sheridan, V. Petseva, L. Adumeau, K. A. Dawson, Multifunctional superparamagnetic nanoparticles with a fluorescent silica shell for the in vitro study of bio-nano interactions at the subcellular scale, Nanoscale 13 (38) (2021) 16324–16338.

[47] T. Uchino, N. Kurumoto, N. Sagawa, Structure and formation mechanism of blue-light-emitting centers in silicon and silica-based nanostructured materials, Phys. Rev. B 73 (23) (2006) 233203.

[48] S.-H. Wu, C.-Y. Mou, H.-P. Lin, Synthesis of mesoporous silica nanoparticles, Chem. Soc. Rev. 42 (9) (2013) 3862–3875.

[49] Y. Li, A. Keilbach, M. Kienle, Y. Goto, S. Inagaki, P. Knochel, T. Bein, Hierarchically structured biphenylene-bridged periodic mesoporous organosilica, J. Mater. Chem. 21 (43) (2011) 17338–17344.

[50] H. Hosono, Y. Abe, H. Imagawa, H. Imai, K. Arai, Experimental evidence for the Si-Si bond model of the 7.6-eV band in ${mathrm{SiO}}_{2}$ glass, Phys. Rev. B 44 (21) (1991) 12043–12045.

[51] F. Musso, P. Ugliengo, X. Solans-Monfort, M. Sodupe, Periodic DFT study of radical species on crystalline silica surfaces, J. Phys. Chem. C 114 (39) (2010) 16430–16438.

[52] Y.-I. Matsushita, A. Oshiyama, Structural stability and energy levels of carbon-related defects in amorphous SiO2 and its interface with SiC, Jpn. J. Appl. Phys. 57 (12) (2018) 125701.

[53] H. Yuasa, S. Kuno, Intersystem crossing mechanisms in the room temperature phosphorescence of crystalline organic compounds, Bull. Chem. Soc. Jpn. 91 (2) (2018) 223–229.

[54] Q. Zhang, Y. Ji, Z. Chen, D. Vella, X. Wang, Q.-H. Xu, Y. Li, G. Eda, Controlled aqueous synthesis of 2D hybrid perovskites with bright room-temperature long-lived luminescence, J. Phys. Chem. Lett. 10 (11) (2019) 2869–2873.

[55] J. Yin, R. Naphade, L. Gutiérrez Arzaluz, J.-L. Brédas, O.M. Bakr, O.F. Mohammed, Modulation of broadband emissions in two-dimensional ⟨100⟩-oriented ruddlesden-popper hybrid perovskites, ACS Energy Lett. 5 (7) (2020) 2149–2155.

[56] H. Hu, Y. Liu, Z. Xie, Z. Xiao, G. Niu, J. Tang, Observation of defect luminescence in 2D Dion-Jacobson perovskites, Adv. Opt. Mater. 9 (24) (2021) 2101423.

[57] K.N. Sugahara, T. Teesalu, P.P. Karmali, V.R. Kotamraju, L. Agemy, O.M. Girard, D. Hanahan, R.F. Mattrey, E. Ruoslahti, Tissue-penetrating delivery of compounds and nanoparticles into tumors, Cancer Cell 16 (6) (2009) 510–520.

[58] G.-H. Kim, G. Lee, M.-H. Kang, M. Kim, Y. Jin, S. Beck, J. Cheon, J. Sung, J. Joo, Luminescent silicon nanoparticles for distinctive tracking of cellular targeting and trafficking, Faraday Discuss. 222 (2020) 304–317.

[59] C.D. Spicer, C. Jumeaux, B. Gupta, M.M. Stevens, Peptide and protein nanoparticle conjugates: versatile platforms for biomedical applications, Chem. Soc. Rev. 47 (10) (2018) 3574–3620.

[60] J. Yoo, K. Kim, S. Kim, H.H. Park, H. Shin, J. Joo, Tailored polyethylene glycol grafting on porous nanoparticles for enhanced targeting and intracellular siRNA delivery, Nanoscale 14 (39) (2022) 14482–14490.

[61] T. Teesalu, K.N. Sugahara, V.R. Kotamraju, E. Ruoslahti, C-end rule peptides mediate neuropilin-1-dependent cell, vascular, and tissue penetration, Proc. Natl. Acad. Sci. U.S.A. 106 (38) (2009) 16157–16162.

[62] S.M.A. Fateminia, Z. Mao, S.D. Xu, Z.Y. Yang, Z.G. Chi, B. Liu, Organic nanocrystals with bright red persistent room-temperature phosphorescence for biological applications, Angew Chem Int Edit 56 (40) (2017) 12160–12164.

[63] S.K. Li, R. Chang, L.Y. Zhao, R.R. Xing, J.C.M. van Hest, X.H. Yan, Two-photon nanoprobes based on bioorganic nanoarchitectonics with a photo-oxidation enhanced emission mechanism, Nat. Commun. 14 (1) (2023).

[64] A. Nicol, R.T.K. Kwok, C.P. Chen, W.J. Zhao, M. Chen, J.A. Qu, B.Z. Tang, Ultrafast delivery of aggregation-induced emission nanoparticles and pure organic phosphorescent nanocrystals by saponin encapsulation, J. Am. Chem. Soc. 139 (41) (2017) 14792–14799.

[65] X. Wang, W.J. Sun, H.F. Shi, H.L. Ma, G.W. Niu, Y.X. Li, J.H. Zhi, X.K. Yao, Z. C. Song, L. Chen, S. Li, G.H. Yang, Z.X. Zhou, Y.X. He, S.L. Qu, M. Wu, Z. Zhao, C. Z. Yin, C.Y. Lin, J. Gao, Q.Y. Li, X. Zhen, L. Li, X.Y. Chen, X.G. Liu, Z.F. An, H. M. Chen, W. Huang, Organic phosphorescent nanoscintillator for low-dose X-ray-induced photodynamic therapy, Nat. Commun. 13 (1) (2022).

[66] W.L. Zhou, Y. Chen, Q.L. Yu, H.Y. Zhang, Z.X. Liu, X.Y. Dai, J.J. Li, Y. Liu, Ultralong purely organic aqueous phosphorescence supramolecular polymer for targeted tumor cell imaging, Nat. Commun. 11 (1) (2020).

[67] Y. Park, J. Yoo, M.-H. Kang, W. Kwon, J. Joo, Photoluminescent and biodegradable porous silicon nanoparticles for biomedical imaging, J. Mater. Chem. B 7 (41) (2019) 6271–6292.

[68] Q. Yin, A. Pan, B. Chen, Z. Wang, M. Tang, Y. Yan, Y. Wang, H. Xia, W. Chen, H. Du, M. Chen, C. Fu, Y. Wang, X. Yuan, Z. Lu, Q. Zhang, Y. Wang, Quantitative imaging of intracellular nanoparticle exposure enables prediction of nanotherapeutic efficacy, Nat. Commun. 12 (1) (2021) 2385.

[69] S.H. Cheng, F.C. Li, J.S. Souris, C.S. Yang, F.G. Tseng, H.S. Lee, C.T. Chen, C. Y. Dong, L.W. Lo, Visualizing dynamics of sub-hepatic distribution of nanoparticles using intravital multiphoton fluorescence microscopy, ACS Nano 6 (5) (2012) 4122–4131.

[70] R.P. Rastogi, A. Richa, M.B. Kumar, R.P.S. Tyagi, Molecular mechanisms of ultraviolet radiation-induced DNA damage and repair, J. Nucleic Acids 2010 (2010) 592980.

[71] X. Zhen, Y. Tao, Z. An, P. Chen, C. Xu, R. Chen, W. Huang, K. Pu, Ultralong phosphorescence of water-soluble organic nanoparticles for in vivo afterglow imaging, Adv Mater 29 (33) (2017).

[72] H.Q. Gao, Z.Y. Gao, D. Jiao, J.T. Zhang, X.L. Li, Q.Y. Tang, Y. Shi, D. Ding, Boosting room temperature phosphorescence performance by alkyl modification for intravital orthotopic lung tumor imaging, Small 17 (22) (2021).

[73] F.M. Xiao, H.Q. Gao, Y.X. Lei, W.B. Dai, M.C. Liu, X.Y. Zheng, Z.X. Cai, X.B. Huang, H.Y. Wu, D. Ding, Guest-host doped strategy for constructing ultralong-lifetime near-infrared organic phosphorescence materials for bioimaging, Nat. Commun. 13 (1) (2022).

[74] J. Yoon, Hyperspectral imaging for clinical applications, BioChip J. 16 (1) (2022) 1–12.

[75] D. Kudaibergen, H.S. Park, J. Park, G.B. Im, J.R. Lee, Y.K. Joung, S.H. Bhang, J. H. Kim, Silica-based advanced nanoparticles for treating ischemic disease, Tissue Eng. Regener. Med. 20 (2) (2023) 177–198.

[76] G. Kresse, J. Hafner, Norm-conserving and ultrasoft pseudopotentials for first-row and transition elements, J. Phys. Condens. Matter 6 (40) (1994) 8245–8257.

[77] G. Kresse, J. Furthmüller, Efficient iterative schemes for ab initio total-energy calculations using a plane-wave basis set, Phys. Rev. B 54 (16) (1996) 11169–11186.

[78] J.P. Perdew, K. Burke, M. Ernzerhof, Generalized gradient approximation made simple, Phys. Rev. Lett. 77 (18) (1996) 3865–3868.

[79] H.J. Monkhorst, J.D. Pack, Special points for Brillouin-zone integrations, Phys. Rev. B 13 (12) (1976) 5188–5192.

[80] K. Momma, F. Izumi, VESTA 3 for three-dimensional visualization of crystal, volumetric and morphology data, J. Appl. Cryst. 44 (6) (2011) 1272–1276.

[81] M. Fox, Optical Properties of Solids, Oxford University Press, 2001.

[82] B. Peng, H. Zhang, H. Shao, Y. Xu, R. Zhang, H. Zhu, The electronic, optical, and thermodynamic properties of borophene from first-principles calculations, J. Mater. Chem. C 4 (16) (2016) 3592–3598.

[83] Y. An, M. Chen, Q. Xue, W. Liu, Preparation and self-assembly of carboxylic acid-functionalized silica, J. Colloid Interface Sci. 311 (2) (2007) 507–513.

[84] S. Roh, Y. Jang, J. Yoo, H. Seong, Surface modification strategies for biomedical applications: enhancing cell-biomaterial interfaces and biochip performances, BioChip J. 17 (2) (2023) 174–191.